



Nanomechanical mapping of the osteochondral interface with contact resonance force microscopy and nanoindentation [☆]

Sara E. Campbell ^{a,*}, Virginia L. Ferguson ^b, Donna C. Hurley ^a

^a Materials Reliability Division, National Institute of Standards and Technology, Boulder, CO 80305, USA

^b Department of Mechanical Engineering, University of Colorado, Boulder, CO 80309, USA

ARTICLE INFO

Article history:

Received 16 March 2012
Received in revised form 3 July 2012
Accepted 30 July 2012
Available online 6 August 2012

Keywords:

AFM
Bone
Cartilage
Nanoindentation
Osteochondral

ABSTRACT

The bone–cartilage, or osteochondral, interface resists remarkably high shear stresses and rarely fails, yet its mechanical characteristics are largely unknown. A complete understanding of this hierarchical system requires mechanical-property information at the length scales of both the interface and the connecting tissues. Here, we combined nanoindentation and atomic force microscopy (AFM) methods to investigate the multiscale mechanical properties across the osteochondral region. The nanoindentation modulus M ranged from that of the subchondral bone ($M = 22.8 \pm 1.8$ GPa) to that of hyaline articular cartilage embedded in PMMA ($M = 5.7 \pm 1.0$ GPa) across a narrow transition region <5 μm wide. Contact resonance force microscopy (CR-FM), which measures the frequency and quality factor of the AFM cantilever's vibrational resonance in contact mode, was used to determine the relative storage modulus and loss tangent of the osteochondral interface. With better spatial resolution than nanoindentation, CR-FM measurements indicated an even narrower interface width of 2.3 ± 1.2 μm . Furthermore, CR-FM revealed a 24% increase in the viscoelastic loss tangent from the articular calcified cartilage into the PMMA-embedded hyaline articular cartilage. Quantitative backscattered electron imaging provided complementary measurement of mineral content. Our results provide insight into the multiscale functionality of the osteochondral interface that will advance understanding of disease states such as osteoarthritis and aid in the development of biomimetic interfaces.

Published by Elsevier Ltd. on behalf of Acta Materialia Inc.

1. Introduction

Within the articular joint, forces are transmitted across the mechanically dissimilar layers of tissue that comprise the osteochondral region: rigid subchondral bone (SCB), a thin (~ 50 μm to 100s μm) layer of articular calcified cartilage (ACC), and compliant hyaline articular cartilage (HAC). In vivo loading of the osteochondral region generates high stresses [1,2]. In particular, a stress concentration exists at the leading edge of mineralization, or the tidemark interface, between the mineralized ACC and the unmineralized HAC. Collagen fibers that traverse this interface perpendicularly are thought to dissipate and resist shear stresses [3]. The mineral within the ACC has long been thought to vary in mineral volume fraction to functionally grade properties from the SCB to the HAC [4]. Mineralization of the SCB and ACC often increases with age and altered loading conditions, and likely plays a key role in the development of disease states such as osteoarthritis [5–7]. However, our limited understanding of load transmission and

mechanical properties across the osteochondral region restricts our ability both to understand disease progression and to engineer replacement materials [8].

Past investigations of the osteochondral region have focused primarily on bulk techniques [9,10] that test the combined mechanical response of several tissues (i.e. SCB, ACC and HAC). More recently, nanoindentation studies have probed the mechanical properties of these individual tissues [6,11–13]. However, the leading tidemark interface between ACC and HAC has been studied much less [11], primarily due to the micrometer-scale spatial resolution constraints of nanoindentation. Furthermore, to our knowledge, no studies have examined the spatial distribution of viscoelastic properties within the osteochondral region.

Atomic force microscopy (AFM) methods can provide nanometer-scale mechanical property measurements on a wide array of materials [14–16]. Here, we demonstrate contact resonance force microscopy (CR-FM) [17,18], an AFM method for quantitative mapping of viscoelastic properties across the tidemark interface. The results are compared to complementary information about microscale mechanical properties obtained by nanoindentation and to mineral content obtained by quantitative backscatter electron microscopy (qBSE) imaging. Our results provide new insight into multiscale mechanical properties of the osteochondral region that

[☆] Contribution of NIST, an agency of the US government; not subject to copyright in the US.

* Corresponding author. Tel.: +1 303 497 6570.

E-mail address: sara.campbell@nist.gov (S.E. Campbell).

will help elucidate its functionality in transmitting loads and anchoring HAC to SCB.

2. Materials and methods

2.1. Sample

A femoral head from a New Zealand white rabbit approximately 6 months old was dehydrated in a series of ethanol solutions and embedded in poly(methyl methacrylate) (PMMA). The sample was collected under full Institutional Animal Use and Care Committee approval at the University of Colorado at Boulder. The femoral head was cut in half through the coronal plane with a low-speed saw. A small sample was removed from the anterior section and faced using an ultramicrotome. Use of an ultramicrotome has been shown to minimize the contribution of surface roughness to the measurement of modulus with nanoindentation [19]. The resulting surface had a root mean square roughness of ~13 nm for a 20 μm \times 20 μm region, as measured by tapping mode AFM.

2.2. Nanoindentation

Nanoindentation tests were performed with a commercial instrument (TribolIndenter, Hysitron, Minneapolis, MN). A nanoindentation test array comprising 30 indents \times 8 indents was placed traversing the osteochondral region from the SCB across ACC and into HAC. Indentation tests were performed with a ramp-and-hold method, with constant loading and unloading rates of 100 $\mu\text{N s}^{-1}$. A 30 s hold at maximum load $F_{\text{max}} = 500 \mu\text{N}$ was used to minimize the contribution of creep to the unloading curve [20]. Tests were run with a Berkovich indenter tip calibrated with a fused-silica reference standard. The reduced modulus E^{R} was measured from the slope of the unloading curve (at maximum load) by using a power law fit to 20–95% of the unloading curve with the Oliver–Pharr method [21]. Here, we report the indentation modulus M , which eliminates the need to assume a Poisson's ratio for the sample. M is given by

$$E^{\text{R}} = \left[\frac{1}{M} + \frac{1 - \nu_{\text{t}}^2}{E_{\text{t}}} \right]^{-1} \quad (1)$$

where $E_{\text{t}} = 1140 \text{ GPa}$ is the Young's modulus and $\nu_{\text{t}} = 0.07$ is the Poisson's ratio, respectively, of the diamond indenter tip. Indent sites were located in both scanning electron microscope and light microscope images for classification as falling on SCB, ACC or HAC. Test sites within 5 μm of the leading tidemark interface between ACC and HAC were not included in the determination of the average modulus value for each tissue type (see below). Any test sites falling within 5 μm of a crack or void was discarded from the analysis.

The variables required to determine the minimal spacing between indent sites are listed in Table 1. The use of a fixed maximum load in the nanoindentation measurements resulted in

Table 1
Mechanical testing experimental parameters.

Experimental parameters	Nanoindentation		CR-FM	
	ACC	HAC	ACC	HAC
F_{max} (μN)	500	500	0.4	0.4
Δx (μm)	5	5	0.1–0.5	0.1–0.5
h_{c} (nm)	120–230	200–450	2.5	3.7
a (μm)	0.64	1.26	0.011	0.014
$3a$ (μm)	1.92	3.78	0.033	0.042

Values for the maximum load F_{max} and test spacing Δx used in nanoindentation and CR-FM experimental parameters. Also shown are the corresponding calculated values of contact depth h_{c} , contact radius a at maximum depth and approximate lateral width $3a$ of the elastic zone, as explained in Section 2.

different maximum values of the contact depth h_{c} between and within different tissue types. The range of values for h_{c} measured on each tissue type, as listed in Table 1, are a direct result of tissue mechanical heterogeneity. The critical dimension of interest, namely the contact radius a , can be calculated for a Berkovich tip from the contact depth h_{c} by

$$a = h_{\text{c}} \tan \theta \quad (2)$$

where $\theta = 70.3^\circ$ is the half-included angle of the Berkovich tip. Assuming sphere–plane Hertzian contact mechanics, the stress field is maximal directly beneath the indenter tip and rapidly decreases with increasing depth z into the sample and radial distance r away from the contact [22]. Near the surface ($z = 0$), at $r = 1.5a$ the stress decreases to 10% of the maximum value at $r = 0$ [22,23]. Therefore, the minimum lateral spacing between indentations should be at least $3a$ in order to avoid the influence of neighboring indents. The values of a and $3a$ listed in Table 1 were calculated for the largest h_{c} value in each tissue type. An experimental test spacing $\Delta x = 5 \mu\text{m}$ was chosen based on the value of $3a$ calculated for HAC, which was the largest of the two materials.

2.3. AFM

AFM measurements were performed with a commercial atomic force microscope (MFP-3D, Asylum Research, Santa Barbara, CA) equipped with a specialized cantilever holder containing a damped, high-frequency piezoelectric actuator. Cantilevers were glued directly onto the cantilever holder with fast-setting epoxy. All experiments used rectangular cantilevers with an average manufacturer-specified spring constant $k_{\text{c}} = 13.5 \text{ N m}^{-1}$ and free resonance frequency $f_1^{\text{free}} = 127 \text{ kHz}$ for the first flexural eigenmode. Experimental values of k_{c} for each cantilever were determined with the thermal noise method [24]. CR-FM measurements utilized the second flexural eigenmode with an experimentally measured free resonance frequency $f_2^{\text{free}} = 755 \text{ kHz}$.

Originally developed for quantitative elastic-property imaging of relatively stiff materials [25,26], CR-FM techniques have been recently advanced to allow mapping of viscoelastic properties on more compliant materials [27–29]. Viscoelastic CR-FM involves measuring the frequency f^{CR} and quality factor Q^{CR} of the AFM cantilever's vibrational resonance while the tip is in contact with the sample. With the use of a point mapping procedure [29], f^{CR} and Q^{CR} are determined at each point in an image.

Detailed explanations of viscoelastic CR-FM analysis are provided elsewhere [27–29]. Briefly, the resonance of the cantilever is analyzed with a distributed-mass Euler–Bernoulli beam model. A Kelvin–Voigt element is included to model the response of the tip–sample contact. The element consists of a spring of stiffness k in parallel with a dashpot with damping σ located near the end of the cantilever. With this model for the cantilever dynamics, the normalized tip–sample contact stiffness $\alpha = k/k_{\text{c}}$ and damping coefficient $\beta \propto \sigma$ are determined from the experimental values of f^{CR} and Q^{CR} . Complete mathematical derivations of α and β are too lengthy to include here. Explicit equations to calculate α and β are given in Ref. [29]. Application of sphere–plane Hertzian contact mechanics allows calculation of the reduced storage modulus E^{R} of the unknown sample, as given by [27–29]

$$E^{\text{R}} = E_{\text{cal}}^{\text{R}} (\alpha / \alpha_{\text{cal}})^{3/2} \quad (3)$$

This relation relies on calibration values $E_{\text{cal}}^{\text{R}}$ and α_{cal} [29]. We ultimately report values for the elastic storage modulus M' calculated from

$$E^{\text{R}} = \left[\frac{1}{M'} + \frac{1}{M_{\text{tip}}} \right]^{-1} \quad (4)$$

In our calculations, we assume $M_{\text{tip}} = 165$ GPa for the indentation modulus of the <100> silicon tip. (The further assumption of zero damping in the silicon tip has been made.) Absolute values of M' can be obtained by comparing CR-FM measurements of an unknown sample to those of a material with known M' values [26]. This referencing approach avoids measurements of absolute quantities, such as load, tip radius, contact area and spring constant, which are difficult to perform with sufficient accuracy. For the values of E_{cal}^R and α_{cal} , we used an internal or self-calibration approach. The average value of the indentation modulus M measured by nanoindentation in HAC was used to calculate E_{cal}^R with Eq. (4). For α_{cal} , the normalized contact stiffness of the calibration material, we used the average value of α for each CR-FM image in a region of HAC as far as possible from the tidemark interface and at least $5 \mu\text{m} \times 10 \mu\text{m}$ in size.

In addition to M' , we report values for the loss tangent $\tan \delta$ of the tidemark interface. $\tan \delta$ gives a measurement of the sample damping and is equivalent to E''/E' , where E'' is the loss modulus of the material. Values for $\tan \delta$ were obtained from the CR-FM images with

$$\tan \delta(f) = \frac{2\pi f^{\text{CR}} \sigma}{k} = \frac{\beta f^{\text{CR}} \lambda^2}{\alpha f^{\text{free}}} \quad (5)$$

where λ is a parameter obtained from the cantilever dynamics model. The value of λ depends on the flexural mode chosen [30]; for the lowest three flexural modes, $\lambda = 1.8751, 4.6941$ and 7.8548 . Eq. (5) was obtained by substituting the equivalent CR-FM quantities into an expression for $\tan \delta$ developed for nanoindentation [31,32]. Previous work with viscoelastic CR-FM [27–29] gave expressions for E'' instead of $\tan \delta$. However, use of Eq. (5) is appealing, because it requires no calibration data ($E'_{\text{cal}}, E''_{\text{cal}}$, etc.). It should be noted that measurements of $\tan \delta$ are frequency dependent. The results cited here represent a contact frequency $f^{\text{CR}} \approx 1$ MHz.

CR-FM point maps were acquired with the second flexural eigenmode in different areas of the sample traversing the region from ACC into HAC where the sharp drop in mineralization exists. The tapping mode was used to locate and image the region prior to CR-FM point mapping. Six pairs of contact resonance frequency and quality factor point maps were collected for a total number $n = 27,874$ of data pairs. CR-FM experimental quantities are given in Table 1. For all CR-FM measurements, a constant force $F_{\text{max}} = k_c \cdot d \approx 400$ nN was applied with a triggered set-point corresponding to cantilever deflection $d = 30$ nm. The value of contact radius a given in Table 1 for each tissue type was calculated by assuming sphere-plane Hertzian contact with [22]

$$a = \left(\frac{3F_{\text{max}}R}{4E^R} \right)^{1/3} \quad (6)$$

The average value of E^R was obtained from CR-FM measurements, and the tip radius of curvature was assumed to be $R = 50$ nm. Again, the quantity $3a$ represents the approximate experimental spatial resolution based on Hertzian contact mechanics [22,23]. The experimental test spacing Δx ranged from 100 nm to 500 nm for various images, substantially larger than the spatial resolution. Methods for accurate scanning with CR-FM are under development to simultaneously reduce data acquisition periods and increase spatial resolution [29]. Finally, the contact depth h_c was calculated from a with [22]

$$h_c = \frac{a^2}{R} \quad (7)$$

2.4. qBSE imaging

qBSE provides images of local changes in mineral content that can be location-matched to measurements of mechanical proper-

ties [6,33,34]. The intensity scale in a qBSE image is proportional to the number of backscattered electrons, which is related to atomic number and, therefore, the sample composition [33,35]. After all mechanical testing was completed, the sample was coated with carbon and imaged in backscatter mode on a field-emission scanning electron microscope (Gemini LEO 1525 FEG-SEM, Carl Zeiss, Thornwood, NY). The sample was imaged after a 1 h warm-up period of the microscope with an accelerating voltage of 20 kV, an aperture of 60 μm , a probe current at the sample surface of ~ 500 pA and a working distance of 15 mm. Concurrent imaging of the sample and calibrated glass reference materials allows for quantification of the mineral volume percent, χ . The glass reference materials were imaged at the beginning and the end, and at 20 min intervals throughout the imaging session. Each image contained 1024×768 pixels and ranged from 400 to 60 μm in size (X-dimension). The imaging time of the sample was minimized, and there was no perceptible damage visible during imaging.

Use of these reference materials has been described in detail elsewhere [36]. Briefly, “low” and “high” glass reference samples with compositions $0.25\text{Li}_2\text{O}-0.30\text{B}_2\text{O}_3-0.45\text{SiO}$ and $0.15\text{Li}_2\text{O}-0.10\text{Rb}_2\text{O}-0.30\text{B}_2\text{O}_3-0.45\text{SiO}$ respectively, were selected to encompass the backscatter intensity of the sample. The qBSE images of the rabbit sample were rescaled such that the intensity values corresponding to those of the low reference sample were set to zero and those of the high reference sample were set to the maximum. From such calibrated images, χ was calculated assuming that the mineralized tissue was a two-phase composite comprising a mineral phase and an organic matrix phase. The mineral component was assumed to be mineralogical hydroxyapatite, $\text{Ca}_{10}(\text{PO}_4)_6(\text{OH})_2$, with a backscatter coefficient $\eta = 0.1815$. The organic portion was estimated as a 1:1 weight percent mixture of collagen and PMMA, with $\eta = 0.089$.

It is important to recognize that the low glass calibration sample used in this study corresponds to a mineral content of $\chi = 16\%$. Therefore, the mineralization of any sample regions with χ below this cutoff value cannot be differentiated. Selection of the low glass calibration sample with $\chi > 10\%$ allows for optimization of the dynamic range of atomic contrast within the mineralized portion of the tissue.

qBSE imaging was performed in the same regions of the sample where the mechanical measurements were made. Identification of the mechanical measurement sites was aided by creating deep ($\sim 2 \mu\text{m}$) marker indents that were visible during qBSE imaging. Upon repeated alignment of images using the marker indent site, we estimate the error in location matching to be less than ± 250 nm. Location-matched line traces were used to compare mechanical property maps to mineralization levels. To compare values of χ for the SCB and ACC tissues, image-processing software (NIH ImageJ, Bethesda, MD, USA, <http://www.rsby.info.nih.gov/ij/>) was used. The average value of χ for each tissue was determined after image thresholding in order to ignore the contribution of pore spaces and the highly mineralized cement line. Inclusion of the cement line as either SCB or ACC tissue would drastically skew the average value of χ .

3. Results and discussion

3.1. Morphology

A qBSE image of the osteochondral region is shown in Fig. 1, where darker regions correspond to areas of higher mineral content. HAC contains no minerals and thus appears white. The highly mineralized cement line (C) that separates the SCB and ACC is visible in Fig. 1, as are examples of Haversian canals (H) and arrested chondrocytes (CH). No significant difference (unpaired

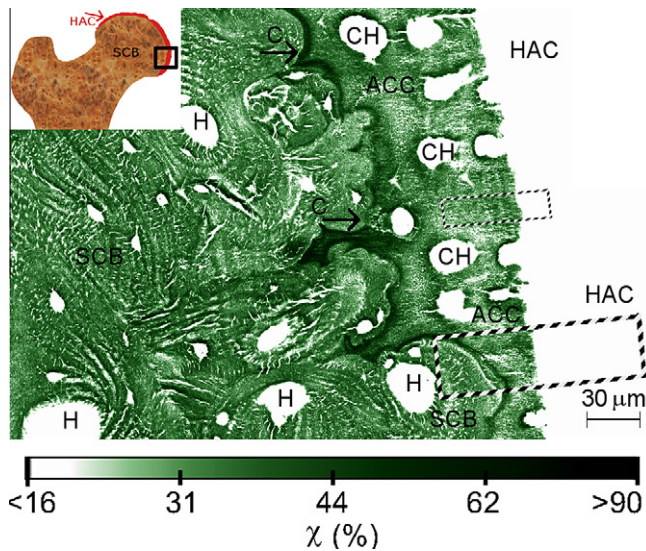


Fig. 1. qBSE image of the rabbit femoral head sample. The color scale gives the mineral volume percent χ obtained from qBSE imaging. The highly mineralized, wavy cement line (C) that divides subchondral bone (SCB) from articular calcified cartilage (ACC) is clearly visible. The hyaline articular cartilage (HAC) contains no mineral and is therefore white in this quantitative image. Examples of Haversian canals (H) and arrested chondrocytes (CH) are also labeled. The dashed lines mark the region of the nanoindentation data in Fig. 3, and the location of the CR-FM data in Fig. 4. The inset shows a schematic of the femur to indicate the sample's anatomical location and orientation. The boxed region represents the entire region removed from the femur for testing.

Student's *t*-test, $p = 0.97$) in mineral content was found between SCB ($\chi = 33.6 \pm 4.2\%$) and ACC ($\chi = 33.0 \pm 5.6\%$).

The region of particular interest in this study is the leading tide-mark that demarcates the border between mineralized cartilage (ACC) and the unmineralized HAC. This region is further referred to as the tidemark interface. It can be seen in Fig. 1 that, at the tide-mark interface, the mineral content decreases over a few micrometers from $\chi = 40\%$ to $\chi < 16\%$. (Recall that our qBSE standards limit the minimal detection to 16% mineral volume fraction. Regions with $\chi \leq 16\%$ are represented in white.) The gradient in mineralization likely contributes to the decrease in mechanical properties across the leading tidemark.

Additionally, the collagen fibers that traverse the interface [3,37] also likely play an important role in transmitting stresses [9,10]. These wavy and parallel, or crimped, collagen fibers are visible in Fig. 2, which contains an image of topography obtained in AFM tapping mode. While crimping is most often observed in tendons or ligaments, it is unclear if the collagen within unmineralized cartilage is crimped in vivo or if distortion resulted from sample dehydration and subsequent shrinkage during processing. Collagen fibers function under tension in vivo [38], suggesting that the crimping could be the result of sample preparation. Similar fibers were visible in most regions imaged prior to collection of mechanical property data. Future studies with optical methods

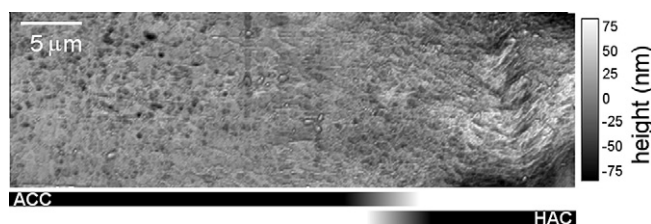


Fig. 2. AFM topography image of the osteochondral interface. Crimping in collagen fibers is evident in HAC.

such as polarized light microscopy or two-photon second harmonic imaging that enable visualization of directionality and prevalence of aligned collagen fibrils could help to clarify this question. Additionally, submicrometer porosity within ACC is evident in Fig. 2.

3.2. Nanoindentation

A nanoindentation map of indentation modulus M across the osteochondral region is shown in Fig. 3a, and the corresponding qBSE image of mineral volume percent χ is given in Fig. 3b. The maps span three materials that compose the osteochondral region: SCB, ACC and HAC. A small but statistically significant (unpaired Student's *t*-test, $p < 0.05$) difference between the average modulus of SCB and ACC was observed: $M(\text{SCB}) = 22.8 \pm 1.6$ GPa for $n = 32$ points, whereas $M(\text{ACC}) = 21.3 \pm 1.8$ GPa for $n = 45$. The average values of M for both SCB and ACC were significantly larger (unpaired Student's *t*-test, $p < 0.001$) than those for the PMMA-embedded HAC, with $M(\text{HAC}) = 5.7 \pm 1.0$ GPa ($n = 131$). It is important to note that the measured values of HAC are almost certainly influenced by the PMMA embedding medium ($M = 5.5$ GPa, obtained by nanoindentation). A further discussion of this point is provided in Section 3.4. Despite the slightly larger value of values of M in SCB compared to ACC, no difference in χ was observed.

ACC requires a higher mineral volume fraction relative to SCB to obtain comparable mechanical properties [6,11]. This is consistent with our slightly lower value of M for ACC than SCB at the same mineral volume fraction. These property differences may result from molecular-level interactions between the mineral and collagen or from variations in crosslinking between type I collagen in bone and type II collagen in ACC. In support of this theory, others have observed a less-well-developed physical connection between mineral particles and collagen in ACC as compared to bone [39]. Alternatively, differences may be caused by exceptional anisotropy resulting from the highly aligned mineralized collagen fibers within the ACC as compared to the less anisotropic bone material [9]. Therefore, the slightly lower values of M we observed for ACC compared to SCB are likely a result of differences in tissue organization as well as molecular level interactions.

As revealed by the representative line scans in Fig. 3a and b, the spatial location of the sharp decrease in M from ACC to HAC corresponds to a region where χ decreases to less than 16%. The transition in modulus occurs abruptly, with no data points of intermediate values. Therefore, we conclude from the nanoindentation results that the interface is less than 5 μm wide. Increased spatial resolution is required to discriminate mechanical property variations across the interface.

In an attempt to improve the spatial resolution of the nanoindentation measurements, several nanoindentation line scans were acquired with 3 μm spacing. However, these scans showed evidence of boundary effects [40], especially in HAC, and thus were considered unreliable. As mentioned above, our nanoindentation instrument is limited to load-controlled operation, resulting in different maximum depths of indentation in different materials. Thus, the lateral spatial resolution differs from region to region. Previous finite element analysis of nanoindentation near an infinitely sharp interface showed that boundary effects can influence measured modulus values at distances up to 10 times the indentation depth for a Berkovich tip [40]. Because the maximum depth h_c in HAC was ~ 450 nm, data within 4.5 μm of either side of the interface could contain errors due to boundary effects. Thus it is not surprising that we observed boundary effects in the line scans with 3 μm spacing but not in the maps with 5 μm spacing. Although we were unable to spatially resolve the interface with maximum-load nanoindentation methods, improved spatial resolution may be

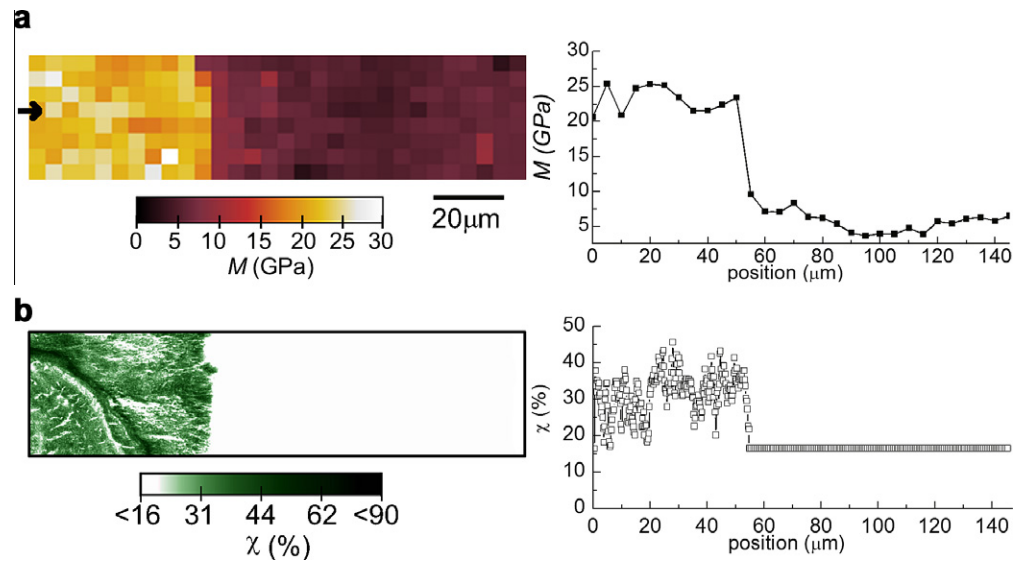


Fig. 3. Maps (left) and corresponding line traces (right) of the osteochondral interface of the rabbit femoral sample. (a) Indentation modulus M obtained from nanoindentation data with $5\ \mu\text{m}$ spacing. (b) Corresponding qBSE values for mineral volume percent χ . Line traces correspond to the single line location at arrow (a). Both images are to the same scale, shown in (a).

possible with the constant-depth-controlled operation available on other nanoindentation systems.

3.3. CR-FM

Higher spatial resolution mechanical mapping across the tide-mark interface was achieved with viscoelastic CR-FM methods. Fig. 4 shows CR-FM results for M' and $\tan \delta$ for the region indicated in Fig. 1. The corresponding AFM height image in Fig. 4a shows that the topography in this region is relatively smooth. Thus we expect minimal topographic effects on the measured values of M' and $\tan \delta$. The line profile (average of four line scans) on the right in Fig. 4b displays a decrease in storage modulus from $M'(\text{ACC}) = 12.1 \pm 0.9\ \text{GPa}$ to $M'(\text{HAC}) = 5.7 \pm 0.2\ \text{GPa}$. By comparing the line scan of M' in Fig. 4b to the corresponding one for χ obtained by qBSE in Fig. 4d, it can be seen that the transition region in M' occurs over the same physical location where the mineral content decreases to less than 16%.

Average storage modulus values $M'(\text{ACC}) = 11.1 \pm 2.4\ \text{GPa}$ ($n = 6676$) and $M'(\text{HAC}) = 6.1 \pm 1.1\ \text{GPa}$ ($n = 7309$) were obtained by evaluation of all CR-FM data at least $5\ \mu\text{m}$ away from the tide-mark interface. Recall that the values of M' were calibrated from a smaller region in HAC, away from the interface, from the average value of $M(\text{HAC})$ obtained by nanoindentation ($M'_{\text{cal}} = 5.7\ \text{GPa}$). Within the ACC, there was a difference of almost a factor of two between the AFM M' of $11.1 \pm 2.4\ \text{GPa}$ and the nanoindentation $M(\text{ACC})$ of $21.3 \pm 1.8\ \text{GPa}$. We performed several independent tests (with large spherical-tip cantilevers, multiple calibration samples, etc.) to verify the observed discrepancy between the measurement methods. The results indicated that it was not an experimental artifact or calibration error.

Transition regions with a steep gradient in storage modulus were observed in every CR-FM map. The six CR-FM maps were taken across a $\sim 1\ \text{cm}$ region of the femoral head. To determine an average interface width, a total of 26 lateral profiles were extracted from the six CR-FM maps of M' . In order to reduce the scatter, each profile represents the average of four adjacent rows of data. For each profile, the interphase upper and lower boundaries were defined as the average value of $M'(\text{ACC})$ minus one standard deviation and the average value of $M'(\text{HAC})$ plus one standard deviation, respectively. The interface width w was defined as the distance

between these boundaries. All the data points falling within the boundaries as defined above for M' are indicated by filled symbols in Fig. 4. The average interface width for all profiles combined was $w = 2.3 \pm 1.2\ \mu\text{m}$. Because the interface width was $< 5\ \mu\text{m}$, it is consistent with our nanoindentation results.

The depths typically probed with CR-FM (see Table 1) imply that boundary effects should influence data only within $\sim 40\ \text{nm}$ of the interface. Therefore, our CR-FM data resolves the interface to the experimental spacing (100–500 nm, depending on the image) without a substantial contribution of boundary effects. However, other effects, such as averaging four rows together, might broaden the measured interface width. Further, the interface contains curvature in three dimensions, indicating that subsurface features may also skew the location or width of the interface. It should be noted that the absolute values of the osteochondral mechanical properties, as well as the exact interface width, are likely to vary with the specific sample's anatomical location and loading history.

All CR-FM maps of $\tan \delta$ indicated an increase in damping when moving from ACC into HAC. For example, in the profile in Fig. 4c, $\tan \delta(\text{ACC}) = 0.071 \pm 0.01$ and $\tan \delta(\text{HAC}) = 0.110 \pm 0.02$. The average values obtained for all images combined were $\tan \delta(\text{ACC}) = 0.066 \pm 0.04$ for $n = 6676$ and $\tan \delta(\text{HAC}) = 0.087 \pm 0.03$ for $n = 7309$. However, in contrast to the results for M' , $\tan \delta$ displayed no sharp transition at the interface. Instead, a more gradual increase in $\tan \delta$ began at the edge of the interface and proceeded toward the articular surface. The gradient in damping properties is not only related to the mineral content but is also likely to depend on the degree of collagen organization. Collagen fibers traverse the tide-mark interface from within the ACC, where they are tightly bound by the minerals across to HAC with no mineral to stiffen the fibers. Further from the interface, the fibers are likely to be less constrained, which may promote damping and explain the increase in $\tan \delta$ away from the interface.

CR-FM measurements of $\tan \delta$ are independent, as they rely on no referencing or calibration technique (unlike those for M'). Comparison of CR-FM $\tan \delta$ measurements to those made by dynamic mechanical analysis (DMA) are complicated by the sample preparation (PMMA embedding) and the high test frequencies of CR-FM ($\sim 1\ \text{MHz}$) compared to DMA ($\sim 1\ \text{Hz}$). Despite these limitations, DMA measurements on wet HAC ($\tan \delta = 0.086 \pm 0.01$) [41] and wet bone ($\tan \delta = 0.040 \pm 0.07$) [42] compared well with our results

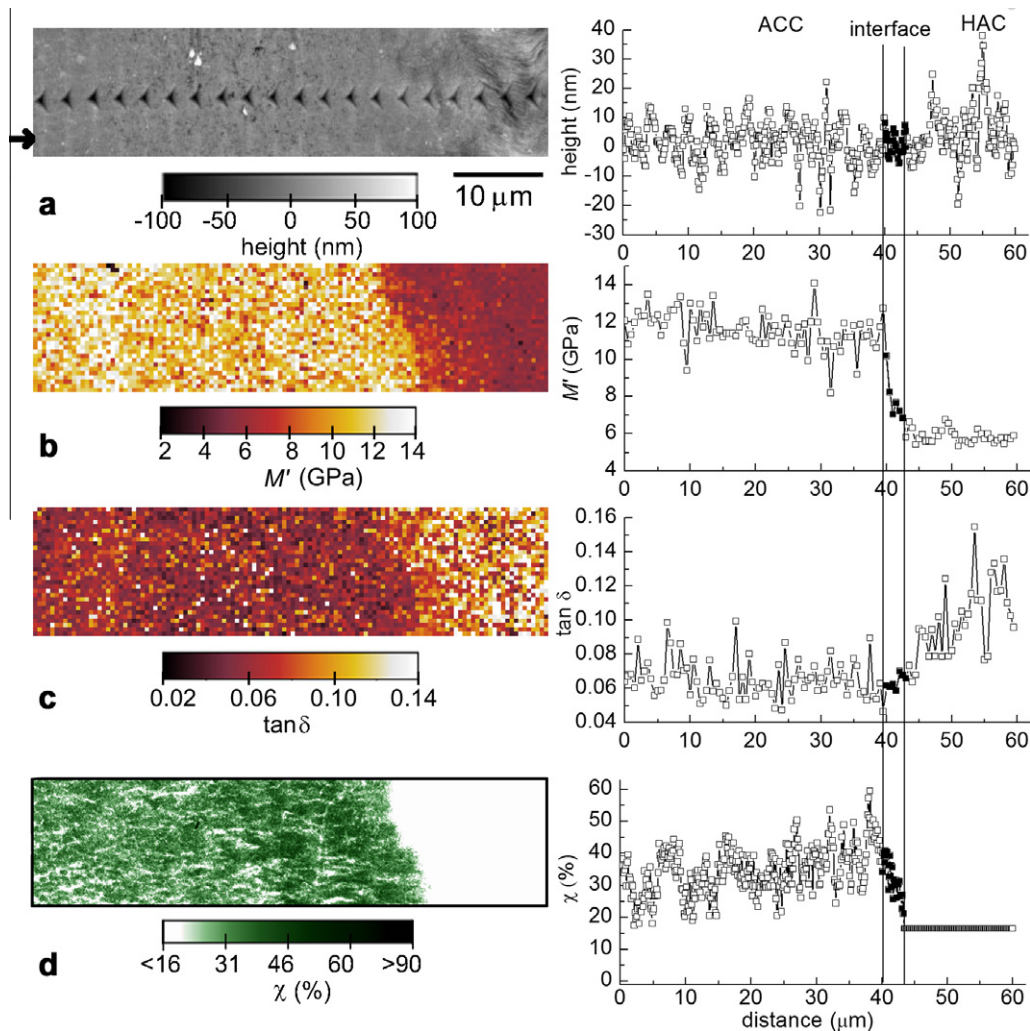


Fig. 4. Maps (left) and corresponding line profiles (right) of the osteochondral interface. (a) AFM intermittent-contact-mode topography image with visible nanoindentation sites. (b) Storage modulus M' and (c) loss tangent $\tan \delta$ from viscoelastic CR-FM point maps. (d) qBSE mineral volume percent χ . Line profiles correspond to the location indicated by the black arrow in (a). The traces in (b) and (c) represent the average of four rows. The interface region determined by the gradient in M' is indicated by the filled symbols in each plot. All images are to same scale, shown in (a).

on PMMA-embedded HAC and ACC, respectively. No DMA measurements have been made on ACC, perhaps due to the difficulty of sectioning the tissue for bulk testing.

3.4. Sample considerations

In interpreting our results, it is important to consider the possible effects of sample preparation. Previous work indicates that the indentation modulus of dehydrated mineralized tissues is typically $\sim 30\%$ less than wet tissue [43]. However, mechanical property variations between tissue types [43], as well as mineral micro- and nanostructure [44], are preserved with ethanol dehydration. While PMMA ($M = 5.5$ GPa) embedding has little effect on the mechanical properties of the mineralized tissue (SCB, ACC) [45], it contributes substantially to properties measured in the HAC ($M = 5.7$ GPa). Although our absolute values of M' and $\tan \delta$ almost certainly do not represent those of HAC *in vivo*, variations within the tissue as compared to baseline PMMA values directly reflect the underlying microstructural organization and relative differences in mineral composition. For example, PMMA is expected to have a constant value of damping ($\tan \delta$); thus, variations in $\tan \delta$ in HAC are most likely representative of changes in the microstructure. Further, in this study we are primarily concerned with

the transition in properties across the interface, not the absolute values. The measurement of interface width is likely unaffected by PMMA embedding. Future development of new analytical methods to account for fluid-cantilever interactions in CR-FM may allow for testing in fluid. Wet testing without PMMA embedding would allow for measurements of material properties closer to *in vivo* conditions.

Additionally, this study utilized only a single sample, with data taken from a relatively small region of approximately $1 \text{ cm} \times 1 \text{ cm}$ in size that was representative of the tissue across the joint surface. Interface width likely depends on such variables as loading conditions, tissue type, age of the tissue, exercise level, anatomical locations and disease state. For example, nanoindentation testing within the human patella measured an interface $\sim 30 \mu\text{m}$ in width [11], more than 10 times that observed here. However, the use of only one small region in this study allowed us to obtain extensive high-resolution information with several techniques.

3.5. Multiscale considerations

In this study, modulus measurements probed ACC at different length scales. The fundamental difference in testing length scales may explain the nearly factor-of-two difference in the measured

modulus values for CR-FM ($M'(ACC) = 11.1 \pm 2.4$ GPa) and nanoindentation ($M'(ACC) = 21.3 \pm 1.8$ GPa). Assuming Hertzian contact, the probed volume of material is approximately $3a$ in depth and diameter. Under the experimental conditions used here, the values of $3a$ for nanoindentation and CR-FM are $\sim 1.9 \mu\text{m}$ and ~ 33 nm, respectively (see Table 1). Thus, AFM-based techniques such as CR-FM probe the mechanical response of the tissues at nanometer length scales similar to that of multiple mineral platelets (roughly $1 \text{ nm} \times 10 \text{ nm} \times 15 \text{ nm}$) and smaller than that of the collagen fibers (diameter approximately 100–200 nm) [46]. In contrast, nanoindentation probes lateral lengths that are 10 times larger than the diameter of a collagen fiber. Therefore, nanoindentation mechanically probes the network of mineralized collagen fibers while CR-FM probes individual mineralized collagen fibers. Similar behavior was observed in wet cartilage [47], where AFM force-displacement measurements with a tip ~ 20 nm in radius yielded stiffness values one-sixth of that determined with a $10 \mu\text{m}$ tip.

CR-FM probes a contact area with a radius of ~ 33 nm, which encompasses the width of multiple mineral platelets. The measured interface width of $w = 2.3 \pm 1.2 \mu\text{m}$ likely represents a region where the number of mineral platelets decreases toward the edge of mineralization. The edge of the interface might represent the location of the last few mineral platelets which have diffused the furthest into the HAC. This idea is further corroborated by qBSE data, which demonstrated a gradation in mineral content over the interface region. The interface width of $w = 2.3 \pm 1.2 \mu\text{m}$ is substantially narrower than previously thought [3,4,10,11]. For example, many tissue engineers have considered the entire width ($\sim 100 \mu\text{m}$) of ACC to be graded in mineralization and mechanical properties and seek to mimic this structure in engineered osteochondral constructs [48,49]. Our multiscale results provide a new paradigm for the role of mineralization in the functionality of the bone-cartilage interface.

4. Conclusions

In this study we utilized two methods, CR-FM and nanoindentation, to measure multiscale mechanical properties across the osteochondral interface region. Particular focus was placed on the tidemark interface, where high stress concentrations exist during *in vivo* loading conditions. In addition, AFM topography imaging and qBSE imaging were performed to provide complementary data on structural and mineralization properties. With nanoindentation, we observed an abrupt drop in storage modulus from SCB/ACC into HAC. CR-FM enabled quantitative mapping with sufficient spatial resolution to examine the spatial distribution of mechanical properties within the tidemark interface. With viscoelastic CR-FM mapping, we obtained an interface width $w = 2.3 \pm 1.2 \mu\text{m}$ for this particular sample. The modulus gradient across the tidemark interface corresponded with a decreasing trend in mineral content measured by qBSE. CR-FM measured a gradual increase in loss tangent δ across the tidemark interface moving into HAC.

The functionality of the osteochondral interface depends on both the mineral and organic phases. We observed similar modulus values within the SCB and ACC, with a gradation of mineral at the leading tidemark region that corresponded to the transition in mechanical properties from ACC to HAC. In addition, the collagen fibers, which have been shown to perpendicularly traverse the tidemark interface in articular joint tissues, anchor the hyaline cartilage to the underlying ACC and may facilitate load transmission into the supportive mineralized region. The mechanical interface between these two tissues is sharp in the sample examined here. In unpublished results, we have observed a similar abrupt interface between hyaline and mineralized cartilage at the osteochondral interface regions in similarly prepared articular

and cartilaginous joint tissues collected from human, equine, ovine and small animal models.

Overall, our multiscale mechanical measurements provide insight into the functionality of the osteochondral region as a robust interface that functions despite being made of highly dissimilar materials. We have demonstrated that the transition between mineralized and unmineralized tissues exists at very small length scales, and that the contrast at this interface is sharp. This work demonstrates the need for further analysis of this fascinating region to determine the role played by collagen fibrils and how osmotic pressure and hydrated macromolecules (e.g. glycosaminoglycans) within the hyaline cartilage serve to facilitate function and prevent osteochondral interface failure. This work also highlights the need for an improved understanding of the precise relationship between mineralization patterns within calcified cartilage and extrinsic factors such as loading conditions, tissue type, age of the tissue, exercise level, anatomical locations and disease state. An improved understanding of this complex anatomical region will enable improved tissue engineering strategies for osteochondral defect repair and treatment of joint disease.

Acknowledgements

We thank Jason Killgore (NIST and University of Colorado-Boulder) for developing the CR-FM point mapping program used for data collection in this work. We also thank Petra Homer (Department of Pathology, University of Colorado-Denver) for assistance with the ultramicrotome sectioning. This work was performed while S.E.C. held a National Research Council Associateship Award at NIST. V.L.F. is grateful for funding by the National Science Foundation CAREER Award (NSF#1055989) and the University of Colorado Innovative Grant Program in support of this work. Commercial equipment, instruments or materials are identified only in order to adequately specify certain procedures. In no case does such identification imply recommendation or endorsement by the National Institute of Standards and Technology, nor does it imply that the products identified are necessarily the best available for the purpose.

Appendix A. Figures with essential colour discrimination

Certain figures in this article, particularly Figs. 1, 3, and 4, are difficult to interpret in black and white. The full colour images can be found in the on-line version, at <http://dx.doi.org/10.1016/j.actbio.2012.07.042>.

References

- [1] Eberhardt AW, Keer LM, Lewis JL, Vithoontien V. An analytical model of joint contact. *J Biomech Eng-T ASME* 1990;112:407–13.
- [2] Wong M, Carter DR. Articular cartilage functional histomorphology and mechanobiology: a research perspective. *Bone* 2003;33:1–13.
- [3] Redler I, Mow VC, Zimny ML, Mansell J. The ultrastructure and biomechanical significance of the tidemark of articular cartilage. *Clin Orthop Relat Res* 1975;112:357–62.
- [4] Seidi A, Ramalingam M, Elloumi-Hannachi I, Ostrovidov S, Khademhosseini A. Gradient biomaterials for soft-to-hard interface tissue engineering. *Acta Biomater* 2011;7:1441–51.
- [5] O'Connor KM. Unweighting accelerates tidemark advancement in articular cartilage at the knee joint of rats. *J Bone Miner Res* 1997;12:580–9.
- [6] Ferguson VL, Bushby AJ, Boyde A. Nanomechanical properties and mineral concentration in articular calcified cartilage and subchondral bone. *J Anat* 2003;203:191–202.
- [7] Oegema TR, Carpenter RJ, Hofmeister F, Thompson RC. The interaction of the zone of calcified cartilage and subchondral bone in osteoarthritis. *Microsc Res Tech* 1997;37:324–32.
- [8] Yang PJ, Temenoff JS. Engineering orthopedic tissue interfaces. *Tissue Eng Pt B-Rev* 2009;15:127–41.
- [9] Broom ND, Poole CA. A functional-morphological study of the tidemark region of articular cartilage maintained in a non-viable physiological condition. *J Anat* 1982;135:65–82.

- [10] Mente PL, Lewis JL. Elastic modulus of calcified cartilage is an order of magnitude less than that of subchondral bone. *J Orthop Res* 1994;12:637–47.
- [11] Gupta HS et al. Two different correlations between nanoindentation modulus and mineral content in the bone–cartilage interface. *J Struct Biol* 2005;149:138–48.
- [12] Ferguson VL, Bushby AJ, Firth EC, Howell PGT, Boyde A. Exercise does not affect stiffness and mineralisation of third metacarpal condylar subarticular calcified tissues in 2 year old thoroughbred racehorses. *Eur Cells Mater* 2008;16:40–6.
- [13] Franke O et al. Mechanical properties of hyaline and repair cartilage studied by nanoindentation. *Acta Biomater* 2007;3:873–81.
- [14] Butt HJ, Cappella B, Kappl M. Force measurements with the atomic force microscope: technique, interpretation and applications. *Surf Sci Rep* 2005;59:1–152.
- [15] Rosa-Zeiser A, Weilandt E, Hild S, Marti O. The simultaneous measurement of elastic, electrostatic and adhesive properties by scanning force microscopy: pulsed-force mode operation. *Meas Sci Technol* 1997;8:1333–8.
- [16] Radmacher M, Tilmann RW, Gaub HE. Imaging viscoelasticity by force modulation with the atomic force microscope. *Biophys J* 1993;64:735–42.
- [17] Rabe U, Amelio S, Kopycinska M, Hirsekorn S, Kempf M, Goken M, et al. Imaging and measurement of local mechanical material properties by atomic force acoustic microscopy. *Surf Interf Anal* 2002;33:65–70.
- [18] Hurley DC, Kopycinska-Müller M, Kos AB. Mapping mechanical properties on the nanoscale using atomic-force acoustic microscopy. *JOM* 2007;59:23–9.
- [19] Xu J, Rho JY, Mishra SR, Fan Z. Atomic force microscopy and nanoindentation characterization of human lamellar bone prepared by microtome sectioning and mechanical polishing technique. *J Biomed Mater Res A* 2003;67A:719–26.
- [20] Feng G, Ngan AHW. Effects of creep and thermal drift on modulus measurement using depth-sensing indentation. *J Mater Res* 2002;17:660–8.
- [21] Oliver WC, Pharr GM. An improved technique for determining hardness and elastic modulus using load and displacement sensing indentation experiments. *J Mater Res* 1992;7:1564–83.
- [22] Johnson KL. *Contact mechanics*. Cambridge: Cambridge University Press; 1985.
- [23] Hurley D. Contact resonance force microscopy techniques for nanomechanical measurements. In: Bhushan B, Fuchs H, editors. *Applied scanning probe methods XI*. Berlin: Springer; 2009. p. 97–138.
- [24] Hutter JL, Bechhoefer J. Calibration of atomic-force microscope tips. *Rev Sci Instrum* 1993;64:1868–73.
- [25] Kopycinska-Müller M et al. Quantitative evaluation of elastic properties of nano-crystalline nickel using atomic force acoustic microscopy. *Z Phys Chem* 2008;222:471–98.
- [26] Hurley DC, Shen K, Jennett NM, Turner JA. Atomic force acoustic microscopy methods to determine thin-film elastic properties. *J Appl Phys* 2003;94:2347–54.
- [27] Yuya PA, Hurley DC, Turner JA. Contact-resonance atomic force microscopy for viscoelasticity. *J Appl Phys* 2008;104:074916.
- [28] Yuya PA, Hurley DC, Turner JA. Relationship between Q-factor and sample damping for contact resonance atomic force microscope measurement of viscoelastic properties. *J Appl Phys* 2011;109:113528.
- [29] Killgore JP et al. Viscoelastic property mapping with contact resonance force microscopy. *Langmuir* 2011;27:13983–7.
- [30] Rabe U, Amelio S, Kester E, Scherer V, Hirsekorn S, Arnold W. Quantitative determination of contact stiffness using atomic force acoustic microscopy. *Ultrasonics* 2000;38:430–7.
- [31] Loubet JL, Oliver WC, Lucas BN. Measurement of the loss tangent of low-density polyethylene with a nanoindentation technique. *J Mater Res* 2000;15:1195–8.
- [32] Asif SAS, Wahl KJ, Colton RJ, Warren OL. Quantitative imaging of nanoscale mechanical properties using hybrid nanoindentation and force modulation. *J Appl Phys* 2001;90:1192–200.
- [33] Boyde A, Elliott JC, Jones SJ. Stereology and histogram analysis of backscattered electron images: age changes in bone. *Bone* 1993;14:205–10.
- [34] Roschger P, Fratzl P, Eschberger J, Klaushofer K. Validation of quantitative backscattered electron imaging for the measurement of mineral density distribution in human bone biopsies. *Bone* 1998;23:319–26.
- [35] Howell PGT, Boyde A. Monte Carlo simulation of electron backscattering from compounds with low mean atomic number. *Scanning* 1998;20:45–9.
- [36] Campbell SE, Geiss RH, Feller SA, Ferguson VL. Tunable glass reference materials for quantitative backscatter electron imaging of mineralized tissues. *J Mater Res* submitted for publication. <http://dx.doi.org/10.1557/jmr.2012.266>.
- [37] Bullough P, Goodfellow J. The significance of the fine structure of articular cartilage. *J Bone Joint Surg Br* 1968;50B:852–7.
- [38] Mow VC, Ratcliffe A, Poole AR. Cartilage and diarthrodial joints as paradigms for hierarchical materials and structures. *Biomaterials* 1992;13:67–97.
- [39] Duer MJ, Frisic T, Murray RC, Reid DG, Wise ER. The mineral phase of calcified cartilage: its molecular structure and interface with the organic matrix. *Biophys J* 2009;96:3372–8.
- [40] Zhao Y, Ovaert TC. Error estimation of nanoindentation mechanical properties near a dissimilar interface via finite element analysis and analytical solution methods. *J Mater Res* 2010;25:2308–16.
- [41] Fulcher GR, Hukins DWL, Shepherd DET. Viscoelastic properties of bovine articular cartilage attached to subchondral bone at high frequencies. *BMC Musculoskelet Disord* 2009;10:1–7.
- [42] Yamashita J, Li XO, Furman BR, Rawls HR, Wang XD, Agrawal CM. Collagen and bone viscoelasticity: a dynamic mechanical analysis. *J Biomed Mater Res A* 2002;63:31–6.
- [43] Hengsberger S, Kulik A, Zysset P. Nanoindentation discriminates the elastic properties of individual human bone lamellae under dry and physiological conditions. *Bone* 2002;30:178–84.
- [44] Fratzl P et al. Mineral crystals in calcified tissues – a comparative study by SAXS. *J Bone Miner Res* 1992;7:329–34.
- [45] Oyen ML, Ko CC, Bembey AK, Bushby AJ, Boyde A. Nanoindentation and finite element analysis of resin-embedded bone samples as a three-phase composite material. *Mater Res Soc Symp P* 2005;874:L1.7.1–6.
- [46] Revenko I, Sommer F, Minh DT, Garrone R, Franc JM. Atomic force microscopy study of the collagen fibre structure. *Biol Cell* 1994;80:67–9.
- [47] Loparic M et al. Micro- and nanomechanical analysis of articular cartilage by indentation-type atomic force microscopy: validation with a gel–microfiber composite. *Biophys J* 2010;98:2731–40.
- [48] Harley BA, Lynn AK, Wissner-Gross Z, Bonfield W, Yannas IV, Gibson LJ. Design of a multiphase osteochondral scaffold III: fabrication of layered scaffolds with continuous interfaces. *J Biomed Mater Res A* 2010;92A:1078–93.
- [49] Jiang J, Tang A, Ateshian GA, Guo XE, Hung CT, Lu HH. Bioactive stratified polymer ceramic-hydrogel scaffold for integrative osteochondral repair. *Ann Biomed Eng* 2010;38:2183–96.